Article

# Freezing Transitions of Nanoconfined Coarse-Grained Water Show Subtle Dependence on Confining Environment

Qing Lu[†] and John E. Straub*[‡]

[†]Division of Materials Science and Engineering, Boston University, Brookline, Massachusetts 02446, United States
[‡]Department of Chemistry, Boston University, Boston, Massachusetts 02215, United States

S *Supporting Information*

ABSTRACT: The solid-to-liquid phase transition in water nanofilms confined between plates, with varying separations and water–plate interactions ranging from strongly hydrophobic to strongly hydrophilic, was simulated using a coarse-grained monatomic water model (mW) and the generalized replica exchange method (gREM). Extensive gREM simulations combined with the statistical temperature weighted histogram analysis method (ST-WHAM) provide a detailed description of the thermodynamic properties intrinsic to the phase transition, including the transition temperature, isobaric heat capacity, phase change enthalpy, entropy, and their dependence on the interplate distance and the plate–water interaction. The ice structure of water nanofilms was characterized at various conditions using the transverse density profile and the distribution of angles formed by hydrogen-bonded neighboring molecules. Flat bilayer ice was observed to be the dominant solid phase at close interplate distance, while puckered bilayer ice, similar to a slab of ice *Ih*, is the predominant structure at larger interplates. Stable puckered bilayer ice, previously observed to have a low melting point, is observed to have enhanced stability with high melting temperature when confined between hydrophilic plates. These results demonstrate the strong dependence of phase stability and coexistence in nanoconfined systems on the geometry and physical properties of the confining environment.
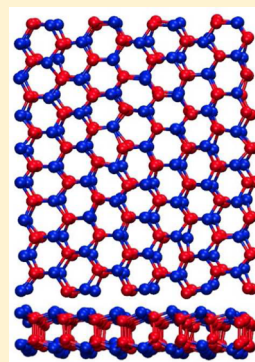
INTRODUCTION

Due to its fundamental importance, water has received a great deal of attention in both experiment and computational studies of its complex and often anomalous behavior. Many atomistic models have been built to reproduce the properties of water in molecular simulations using long-ranged forces (electrostatics) that make simulations intrinsically computational demanding.[1−7] Recently, a coarse-grained monatomic model for water molecules (mW) was developed[8] by Molinero and co-workers to represent water as a single site with three-body potential terms that lead to a tetrahedrality intermediate between carbon and silicon. The mW model captures essential features of the hydrogen bonding in water using a nonbonded angular-dependent term that encourages tetrahedral structure. This potential reproduces the structural, thermodynamic, and dynamic properties of liquid water with comparable or better accuracy than many popular atomistic water models at much less computational cost. mW has been applied to the study of pure bulk water[9−11] and nanoconfined water,[12−14] as well as biological water[15] and clathrate hydrates.[16]

Confined water is present in biological systems and nanoscale materials and is known to possess a variety of structural, dynamic, and thermodynamic properties that differ from bulk water.[12−14,17−22] These are direct results of the interaction with surfaces and/or a truncation of the bulk correlation length and depend on whether the interactions of water with the wall particles are hydrophilic or hydrophobic.[23] Moreover, the geometry of the confinement is also an important factor. The cylindrical nanopore and parallel slit

nanopore are two types of confining geometries used in studies of nanoconfined water.[12,13,17,18,24−29] Experimental evidence of pronounced layering of the water within the confining gap was reported using X-ray reflectivity for water across a narrow gap between cleaved mica surfaces.[30]

This study focuses on bilayer water confined to a slit nanopore made of two infinite parallel plates separated by a fixed distance. Previously, we simulated the solid-to-liquid phase transition in bilayer water as a function of density, demonstrating a variation in the order of the transition from first (at low densities) to second (at high densities).[31] The focus of this study is to probe the effect of varying hydrophilicity of the plates and the plate-to-plate distance on the thermodynamic and structural properties of the nano-confined water film. The transition in confined bilayer water has been shown to be first-order, based on a sharp drop in the potential energy and discontinuity in the diffusion coefficient.[14] However, due to the large latent heat associated with strong first-order phase transitions, it is hard to precisely determine the phase transition temperature using regular MD simulations in canonical ensembles. As such, it is of interest to explore the properties of this transition using a generalized ensemble approach.

Generalized Replica Exchange Method (gREM)[32] is well-suited for the simulation of first-order phase transitions with

large energy gap. It combines the merit of replica exchange paradigm[33−38] and generalized ensemble sampling, and tranforms the unstable or metastable states in the canonical ensemble[39−42] into stable states. Since its development, gREM has been successfully applied to the study of phase transitions in Potts spin systems,[32] an adapted Dzutugov model,[43] Lennard-Jones fluid,[44] bulk water,[45] and nanoconfined water systems.[31] In this study, we employed gREM to simulate the solid-to-liquid phase transition of coarse grained mW water nanofilm. We demonstrate remarkable sensitivity of the transition to the nature of the water-wall interaction, with implications for the understanding of interfacial and nanoconfined water.

■ METHODS AND MATERIALS

System and Force Field. We investigate the state of water confined between both hydrophilic and hydrophobic plates. The mW[8] potential energy consists of a sum of pairwise two-body (Φ_2) and three-body interactions (Φ_3), parametrized as

$$E = \sum_i \sum_{j>i} \Phi_2(r_{ij}) + \sum_i \sum_{j\neq i} \sum_{k>j} \Phi_3(r_{ij}, r_{ik}, \theta_{ijk}) \quad (1)$$

$$\Phi_2(r_{ij}) = A\varepsilon \left[B\left(\frac{\sigma}{r_{ij}}\right)^4 - 1 \right] \exp\left(\frac{\sigma}{r_{ij} - a\sigma}\right) \quad (2)$$

$$\Phi_3(r_{ij}, r_{jk}, \theta_{ijk}) = \lambda\sigma(\cos\theta_{ijk} - \cos\theta_0)^2 \exp\left(\frac{\sigma}{r_{ij} - a\sigma}\right)$$
$$\exp\left(\frac{\sigma}{r_{ik} - a\sigma}\right) \quad (3)$$

with A = 7.049556277, B = 0.6022245584, γ = 1.2, a = 1.8, θ_0 = 109.47°, the tetrahedrality λ = 23.15, the diameter σ_{mW} = 2.3925 Å, and energy scale ε = 6.189 kcal/mol. All intermolecular forces in the mW model vanish at a distance $a\sigma$ = 4.2 Å, making the mW model inherently short-ranged and computationally efficient.

The plates were modeled following prior studies.[12,13,46] One plate consisted of particles arranged in a single-layer triangle lattice with interparticle spacing of 3.2 Å. The interactions between water molecules and particles on the plates were modeled with the two-body potential

$$\Phi_2(r_{ij}) = A\varepsilon_{wp} \left[B\left(\frac{\sigma_{wp}}{r_{ij}}\right)^4 - 1 \right] \exp\left(\frac{\sigma_{wp}}{r_{ij} - a\sigma_{wp}}\right) \quad (4)$$

with σ_{wp} set to 3.2 Å to prevent the diffusion of water molecules into the plate, ε_{wp} modulating the hydrophilicity of the plate, and A and B the same as those for the water−water interactions in the mW model. As the plate−water interaction does not have a three-body potential in this work, the plates do not form directional hydrogen bonds with the water molecules. The hydrophilicity of the plates was characterized by Molinero and co-workers[13] by the simulation of the contact angle of droplets with a flat plate. On the basis of their results, we set the parameters of two hydrophobic plates to be ε_{wp} = 0.2 and 0.3 kcal/mol and the parameters of two hydrophilic plates to be ε_{wp} = 0.5 and 0.7 kcal/mol.

The water nanofilm systems are composed of 256 or 1024 water molecules confined between two parallel plates separated

by a distance D, varying between 8 and 10 Å, with 0.5 Å as the interval. The range of the interplate distance was chosen to form a bilayer water nanofilm as suggested in ref 12. Distances in this study are measured from the centers of the plates. The plates, along with the particles on the plates, have fixed locations in the simulation. A schematic plot of the water nanofilm confined between two parallel plates is shown in Figure 1. The average width of the plate is roughly 55 Å for the system with 256 water molecules and 110 Å for the system with 1024 water molecules.
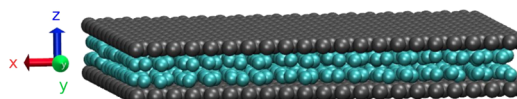

Figure 1. Schematic plot of the water nanofilm confined between two parallel plates. The particles forming the plates are shown in gray, and the water molecules are shown in light blue with x, y, and z axes marked.

The plate−water interactions are governed by eq 2, in which ε_{wp} modulates the hydrophilicity of the plates. We simulated two hydrophobic plates with ε_{wp} = 0.2 and 0.3 kcal/mol and two hydrophilic plates with ε_{wp} = 0.5 and 0.7 kcal/mol. The system is periodically replicated in the x and y directions to model confinement between infinite plates, and the z direction is not subject to periodic boundary conditions. The lateral pressures of water nanofilms are maintained at 1 atm. The lateral dimensions of the water nanofilm are allowed to fluctuate, while the interplate distance is fixed at a certain distance.

Generalized Replica Exchange Method (gREM). We employed the recently developed generalized replica exchange method (gREM)[32] implemented in Monte Carlo simulation to study the solid-to-liquid phase transition in water nanofilms. gREM combines sampling of a generalized noncanonical ensemble with replica exchanges in order to restore the power of the replica exchange paradigm in the vicinity of a strong first-order phase transition. For the convential temperature replica exchange method (tREM), in moving across a strong first-order phase transition, replica exchanges near the transition temperature are severely impaired as the canonical energy or enthalpy distribution functions are disjointed and separated by a large energy or enthalpy gap. gREM bridges the energy/enthalpy gap by controlling the locations of the energy/enthalpy distributions using optimally designed generalized ensemble sampling. A number of studies have demonstrated that gREM achieves comprehensive sampling of phase-coexistence states,[44,45,47] which are inaccessible in a constant-temperature ensemble.

In gREM simulation, each replica α of the system is associated with an effective temperature $T_\alpha(H;\lambda_\alpha)$, H being enthalpy and λ_α being a set of relevant parameters, and samples a configurational space with the generalized ensemble weight $W_\alpha(H;\lambda_\alpha)$, which is determined from the effective temperature through the inverse mapping

$$T_\alpha(H; \lambda_\alpha) = \left[\frac{\partial w_\alpha}{\partial H} \right]^{-1} \quad (5)$$

where $w_\alpha = -\ln W_\alpha$ is the generalized effective potential. The effective temperatures are conveniently parametrized using

linear functions of enthalpy with a uniform slope for all replicas as

$$T_\alpha(H; \lambda_\alpha) = \lambda_\alpha + \gamma_0(H - H_0) \qquad (6)$$

where the control parameter γ_0 is the constant slope, H_0 is a constant offset in the relevant enthalpy range, and λ_α is the T intercept at a chosen H_0. Denoting the lowest and highest temperatures as T_1 and T_M, respectively, the average enthalpies $\tilde{H}_1$ and $\tilde{H}_M$ can be determined by short canonical runs at T_1 and T_M. The value of H_0 can be set as $H_0 = \tilde{H}_1$. The dynamic range of λ_α is determined to be $\lambda_1 = T_1$ and $\lambda_M = T_M - \gamma(\tilde{H}_M - \tilde{H}_1)$, so that the first and Mth effective temperatures cross $[\tilde{H}_1, T_1]$ and $[\tilde{H}_M, T_M]$, respectively. The intermediate values of λ_α ($1 < \alpha < M$) are determined by equally dividing the parameter space as

$$\lambda_\alpha = \lambda_1 + (\alpha - 1)\Delta\lambda \qquad (7)$$

and $\Delta\lambda = (\lambda_M - \lambda_1)/(M - 1)$.

The linear effective temperature of eq 6 produces a generalized ensemble sampling weight

$$W_\alpha(H; \lambda_\alpha) \approx [\lambda_\alpha + \gamma_0(H - H_0)]^{-1/\gamma_0} \qquad (8)$$

which governs the trial moves within one replica and replica exchanges between neighboring replicas. The acceptance probability of a Monte Carlo trial move in configuration space within replica α is

$$A_{g\text{REM}}(\mathbf{x} \to \mathbf{x}') = \min[1, \, e^{w_\alpha(H(\mathbf{x})) - w_\alpha(H(\mathbf{x}'))}] \qquad (9)$$

where $w_\alpha(H) = -\ln W$. The acceptance ratio for replica exchange between neighboring replicas α and $\alpha + 1$ is

$$A_{g\text{REM}}(\alpha; \mathbf{xx}') = \min[1, \, \exp(\Delta_\alpha^x)] \qquad (10)$$

where $\Delta_\alpha^x = w_{\alpha+1}(H(\mathbf{x}')) - w_{\alpha+1}(H(\mathbf{x})) + w_\alpha(H(\mathbf{x})) - w_\alpha(H(\mathbf{x}'))$.

Simulation protocols of the gREM are defined by the following three steps.

(i) Perform short canonical runs for a number of replicas having the temperature equally spaced between the lowest and highest temperatures of interest, T_1 and T_M, to provide relevant data sets for the parameterization of gREM.[32]

(ii) Run the gREM simulation for each replica by making Monte Carlo trial moves in configuration space with the acceptance probability given in eq 9. After all replicas undergo configurational trial moves, randomly choose one pair of neighboring replicas and attempt a replica exchange with the acceptance probability defined by eq 10.

(iii) After the production run is completed, apply the statistical temperature weighted histogram analysis method (ST-WHAM)[48] to join multiple generalized ensemble runs and calculate the entropy estimate and additional observables in the canonical ensemble.

Monte Carlo simulations in configuration space within one replica were arranged in cycles of trial moves including N randomly selected single-particle moves (N is the number of particles in the system), followed by a volume-changing move. A single-particle move is accepted with probability $\min(1, \exp\{-(k_\text{B}T_\alpha)^{-1}[U(r'^N) - U(r^N)]\})$, where T_α is the effective temperature of the replica α, r^N and r'^N are the old and new coordinates of all N particles, and U is the potential energy of the system. The volume-changing move is accepted with probability, $\min(1, \exp\{-(k_\text{B}T_\alpha)^{-1}[H(s^N, V') - H(s^N, V)] + (N + 1)\ln(V'/V)]\})$, where s^N represents the reduced coordinates

scaled by the box dimension, V and V' are the old and new volumes, and H is the enthalpy of the system.[49] When the volume of the water nanofilm is changed from V to V', the length of the water nanofilm, L_x and the width, L_y, are adjusted according to $L_x' = (V'/V)^{1/2}L_x$ and $L_y' = (V'/V)^{1/2}L_y$, while the depth in the z direction remains constant. Consequentially, the coordinates in the x and y directions are adjusted according to $x_i' = (L_x'/L_x)x_i$ and $y_i' = (L_y'/L_y)y_i$, while z coordinates are not affected by a volume change.

The maximum displacements of the single-particle moves and the maximum volume changes were adjusted during the simulation to achieve an average acceptance probability in the range of 45−55%. The equilibrium simulation was performed for 90 000 cycles, and the production simulation was performed for 200 000 cycles. The total CPU time was roughly 120 h on an Intel Xeon E5-2640 processor.

Statistical Temperature Weighted Histogram Analysis Method (ST-WHAM). Because each replica in gREM samples a configurational space with a noncanonical sampling weight, all simulation results should be combined to estimate correct canonical averages via reweighting. The ST-WHAM[48] was used for posterior analysis of gREM simulation results. Unlike the conventional weighted histogram analysis method (WHAM),[50] ST-WHAM does not require iteration to determine the relevant partition function but instead calculates the entropy directly from the quantities determined in gREM, the generalized ensemble sampling weight in each replica, and the associated enthalpy histogram. This approach leads to a substantial acceleration of the data analysis without loss in accuracy, as has been demonstrated in a number of recent applications.[51,52]

ST-WHAM provides an approximate calculation of the entropy through first calculating the inverse statistical temperature, β_S, by

$$\beta_\text{S} = \sum_\alpha f_\alpha(H)\left(\frac{\partial \ln P_\alpha}{\partial H} - \frac{\partial \ln W_\alpha}{\partial H}\right) \qquad (11)$$

where $P_\alpha(H)$ is the enthalpy histogram in replica α and $f_\alpha(H) = P_\alpha(H)/\sum_\alpha P_\alpha(H)$ is the simulated histogram fraction.

Integration of β_S provides an entropy estimate $S(H)$, according to the relationship $\beta_\text{S} = \partial S(H)/\partial H$. Once the entropy is determined, canonical expectation values of any thermodynamic variable may be computed as

$$\langle A(T) \rangle = \frac{\int \text{d}H \, e^{S(H) - \beta E}A(H)}{\int \text{d}H \, e^{S(H) - \beta H}} \qquad (12)$$

and the canonical heat capacity may be estimated through the enthalpy fluctuation as

$$C_\text{p}(T) = \frac{\langle H(T)^2 \rangle - \langle H(T) \rangle^2}{k_\text{B}T^2} \qquad (13)$$

The maximum of the heat capacity is used to define the melting temperature of the ice. The combination of gREM and ST-WHAM allows for the accurate determination of the phase transition temperature between ice and liquid water, as well as the change in enthalpy and entropy.

■ RESULTS AND DISCUSSION

Thermodynamic Properties of the Freezing Transition. We simulated 20 systems with 5 interplate distances, $D = 8, 8.5, 9, 9.5,$ and 10 Å, and 4 different water−plate interaction

strengths, ε_{wp} = 0.2, 0.3, 0.5, and 0.7 kcal/mol. The aim was to carry out an extensive study of the effect of the hydrophilicity of the plates and the plate-to-plate distance on the thermodynamic and structural properties of water nanofilms. Simulations of the solid-to-liquid transition in water nanofilms were performed using gREM. ST-WHAM was used to combine multiple generalized ensemble runs in gREM to determine the inverse statistical temperature and the entropy estimate. The canonical expectation value for the enthalpy and the isobaric heat capacity were computed using eqs 12 and 13. The solid-to-liquid phase transition temperature was determined as the maximum of the heat capacity. Changes in enthalpy, entropy, and the volume of the transition were also computed.

Figure 2 shows the statistical temperature and the canonical temperature of the system with 256 water molecules; D = 9 Å
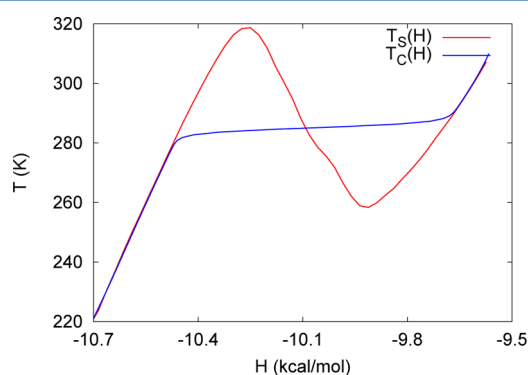

Figure 2. Statistical temperature, $T_S(H)$, and the canonical temperature, $T_C(H)$, of the system with 256 water molecules; D = 9 Å and ε_{wp} = 0.2 kcal/mol, plotted as red and blue lines, respectively.

and ε_{wp} = 0.2 kcal/mol. The statistical temperature shows backbending behavior as an indicator of the strong first-order solid-to-liquid phase transition. In gREM, the S-loop is removed when the temperature is reweighted into the canonical ensemble. The canonical temperature is monotonically increasing as a function of enthalpy in the canonical ensemble.

Figure 3 shows the enthalpy–temperature curves, $H(T)$, and the isobaric heat capacity, $C_p(T)$, of the systems with interplate distance D = 8 Å and four different water–plate interaction strengths, ε_{wp} = 0.2, 0.3, 0.5, and 0.7 kcal/mol. Figure 4 shows isobaric curves of $H(T)$ and $C_p(T)$ of systems with interplate distance D = 10 Å and four different water–plate interaction strengths. In all cases, a sharp peak in $C_p(T)$ and abrupt changes in $H(T)$ are observed, suggesting a first-order phase transition. The enthalpy curve moves downward as ε_{wp} increases, indicating that the enthalpies of both the ice and liquid phases decrease as ε_{wp} increases. At the same time, the enthalpy curve and the heat capacity curve shift to the right as ε_{wp} increases, indicating that the transition temperature increases as ε_{wp} increases.

From the location of the peaks of the isobaric heat capacity curves, the solid-to-liquid phase transition temperatures of all 20 systems were determined. The transition temperatures as a function of the interplate distance D are shown in Figure 5 for systems with ε_{wp} = 0.2, 0.3, 0.5, and 0.7 kcal/mol and with 256 or 1024 water molecules. The transition temperature reaches a maximum at D = 8.5 Å at all values of ε_{wp} and is observed to decrease as the interplate distance increases from 8.5 to 10 Å. The parabolic behavior of the transition temperatures near D = 8.5 Å agrees with previous observations.[12] At a given value D,
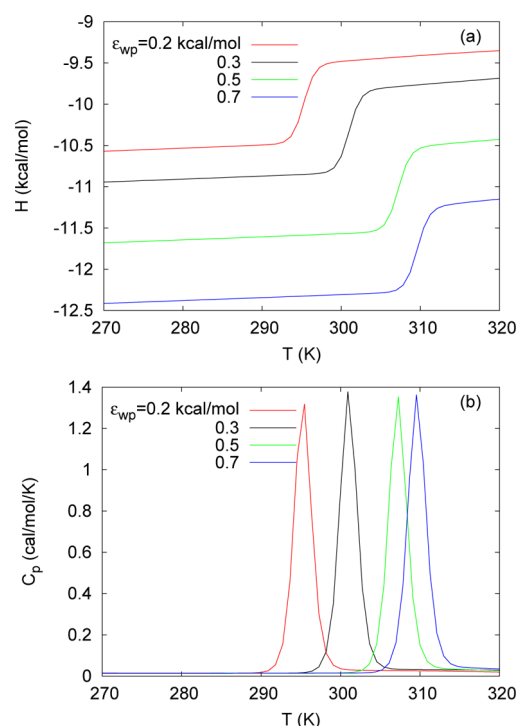

Figure 3. (a) Enthalpy, $H(T)$, and (b) isobaric heat capacity, $C_p(T)$, in canonical ensembles for systems with 256 water molecules; D = 8 Å and ε_{wp} = 0.2, 0.3, 0.5, and 0.7 kcal/mol. The enthalpy and heat capacity curves for systems with 1024 water molecules are shown in the Supporting Information.
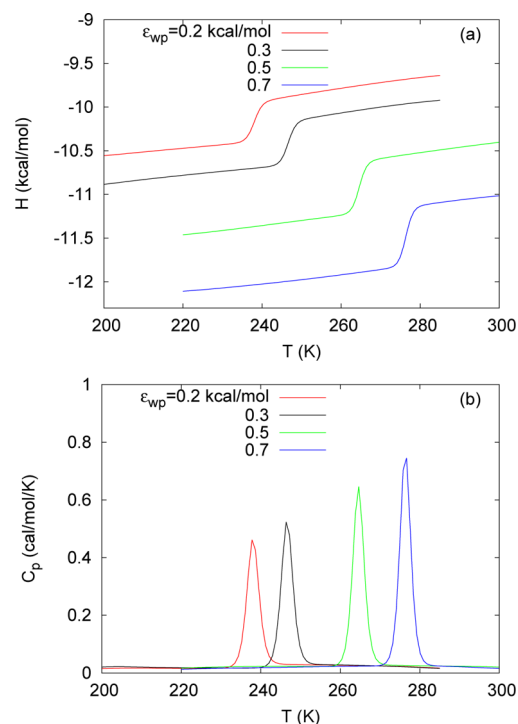

Figure 4. (a) Enthalpy, $H(T)$, and (b) isobaric heat capacity, $C_p(T)$, in canonical ensembles for systems with 256 water molecules; D = 10 Å and ε_{wp} = 0.2, 0.3, 0.5, and 0.7 kcal/mol. The enthalpy and heat capacity curves for systems with 1024 water molecules are shown in the Supporting Information.
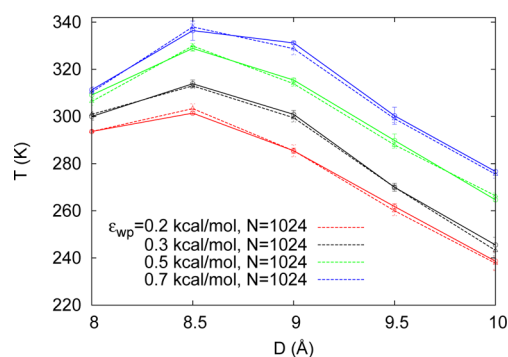
Figure 5. Phase transition temperature of water nanofilms at interplate distance D = 8, 8.5, 9, 9.5, and 10 Å for systems with four different plate−water interaction parameters, ε_{wp} = 0.2, 0.3, 0.5, and 0.7 kcal/mol. The results for systems with 256 and 1024 water molecules are plotted with solid and dashed lines, respectively.

the transition temperature is higher when ε_{wp} of the system is larger. Varying both parameters for interplate distance and the water−plate interaction, D and ε_{wp}, the transition temperature of the water nanofilm is observed to span over a wide range from 240 to 340 K.

Figure 6 shows the change in enthalpy, ΔH, and entropy, ΔS, for the solid-to-liquid transition for different interplate distances D, for systems with four different plate−water interaction parameters, ε_{wp} = 0.2, 0.3, 0.5, and 0.7 kcal/mol. At all distances, within statistical error, the change in enthalpy for systems with hydrophilic plates is higher than that for the corresponding systems with hydrophobic plates. The negative values of ΔV result from the fact that the volume of the water bilayer decreases as it melts. At all distances, the values of ΔV for systems with hydrophilic plates are less negative than those for the corresponding systems with hydrophobic plates, indicating that the volume difference between solid and liquid states decreases. This results from the tendency of the liquid state to expand and increase the contacting areas with the hydrophilic plates favoring the water−plate interaction.

For systems with hydrophobic and hydrophilic plates, as D increases from 8 to 9.5 Å, ΔH and ΔS are observed to decrease monotonically, showing that the differences in enthalpy and entropy of the solid and liquid states are getting smaller as D increases. For systems with strong hydrophilic plates, the results at D = 10 Å do not follow that same trend as ΔS increases, and ΔH maintains a constant value. This is the apparent result of a substantial structural change in the water nanofilm as D increases to 10 Å (discussed below).

The change in entropy, ΔS, for the solid-to-liquid transition can be directly computed using ST-WHAM. We compare $T_m\Delta S$, T_m being the melting temperature, with the phase change enthalpy, ΔH. Figure 7 demonstrates that ΔH agrees very well with $T_m\Delta S$ for water nanofilms confined between plates with ε_{wp} = 0.2, 0.3, 0.5, and 0.7 kcal/mol and separated by varying distances, D. As ΔS, T_m, and ΔH are obtained independently, the close agreement validates our results.

Simulations in this work were performed with a lateral pressure of 1 atm. We estimate dT/dP_L, the slope of the coexistence curve on the temperature−lateral pressure (T−P_L) diagram, given ΔS and ΔV in Figure 6. According to the Clausius−Clapeyron equation for the two-phase boundaries in the quasi-2D system[24] $dT/dP_L = \Delta V/\Delta S$. Tables 1 and 2 list the computed results of dT/dP_L for hydrophobic plates (ε_{wp} = 0.2 kcal/mol) and hydrophilic plates (ε_{wp} = 0.7 kcal/mol)

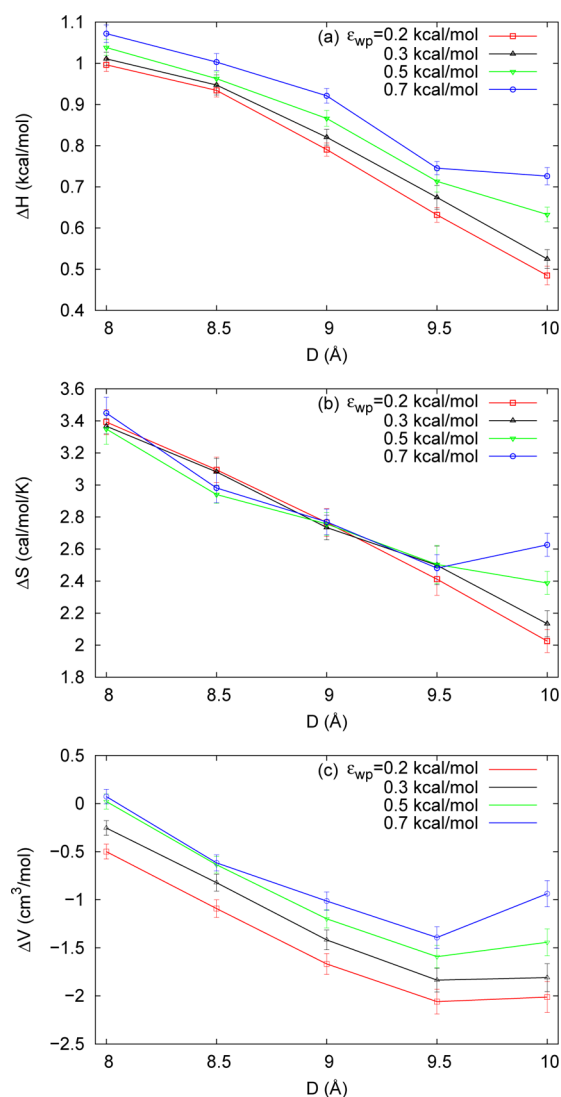**Figure 6.** (a−c) Change in enthalpy ΔH, volume ΔV, and entropy ΔS, for the solid-to-liquid transition in water nanofilms with varying interplate distances, D, for systems with four different plate−water interaction parameters, ε_{wp} = 0.2, 0.3, 0.5, and 0.7 kcal/mol, and 256 water molecules.

separated by varying distances. Most values of dT/dP_L are found to be negative, indicating that the melting temperature decreases with increasing lateral pressure.

The work by Molinero et al.[14] contains data on the melting temperatures of hexagonal bilayer ice at varying lateral pressures, P_L. On the basis of two data points in Table 1 of their work, (P_L = 0, T_m = 297.5 K) and (P_L = 460 MPa, T_m = 237.5 K), dT/dP_L is estimated to be −0.1304 K/MPa. As the plates in their work are hydrophobic plates separated by 8.5 Å, we compared their results to that of hydrophobic plates (ε_{wp} = 0.2 kcal/mol) with D = 8.5 Å, which is dT/dP_L = −0.08426 K/MPa. We consider this to be good agreement. The difference could be attributed to the details of the water−plate interactions used, which were featureless plates modeled by a Lennard-Jones 9−3 potential, unlike the atomistic plates that we used in this work.

Structural Properties of the Nanonconfined Water Film. Structural layering effects induced in the water nanofilm by confinement are examined through the transverse density
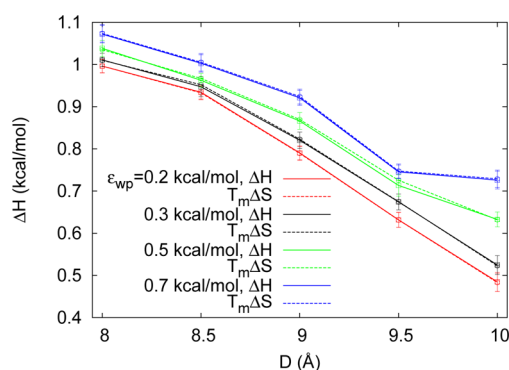
Figure 7. Change in enthalpy, ΔH (plotted with solid lines), compared with $T_m\Delta S$ (plotted with dashed lines), T_m being the melting temperature and ΔS being the change in entropy, for the solid-to-liquid transition in water nanofilms with varying interplate distances, D, for systems with four different plate–water interaction parameters, ε_{wp} = 0.2, 0.3, 0.5, and 0.7 kcal/mol, and 256 water molecules. Note that ΔH should equal $T_m\Delta S$ as ΔG = 0 at equilibrium.

Table 1. Change in Volume, ΔV, Entropy, ΔS, and dT/dP for Hydrophobic Plates (ε_{wp} = 0.2 kcal/mol) Separated by Varying Distances, D, with 256 Water Molecules Confined

D (Å)	ΔV (cm³/mol)	ΔS (cal/mol/K)	dT/dP (K/MPa)
8	−0.65465	3.39301	−0.04611
8.5	−1.07834	3.09493	−0.08327
9	−1.57584	2.76567	−0.13618
9.5	−1.68221	2.41195	−0.16669
10	−1.68263	2.02543	−0.19855

Table 2. Change in Volume, ΔV, Entropy, ΔS, and dT/dP for Hydrophilic Plates (ε_{wp} = 0.7 kcal/mol) Separated by Varying Distances, D, with 256 Water Molecules Confined

D (Å)	ΔV (cm³/mol)	ΔS (cal/mol/K)	dT/dP (K/MPa)
8	−0.38734	3.44927	−0.02684
8.5	−0.79651	2.98097	−0.06386
9	−1.03158	2.76953	−0.08902
9.5	−1.16823	2.48087	−0.11254
10	−1.30915	2.62627	−0.11914

profile (TDP), ρ_z, along the direction z, for ice structures of all 20 systems at T = 220 K (see Figure 8). The zero point of the z-axis is defined as the midpoint between the two plates. The profiles of ρ_z show two peaks symmetric with respect to the midpoint between the plates with interplate distances of D = 8, 8.5, 9, and 9.5 Å, indicating two layers of water molecules confined between plates. When D = 8, 8.5, 9, and 9.5 Å, the peaks in ρ_z assume a Gaussian-like shape centered around z = ±1.4 Å, indicating that both layers are flat (consistent with the 2B structure in ref 12). Meanwhile, the height of the peaks diminishes as D increases from 8 to 9.5 Å, indicating that the solid state becomes less organized at a larger interplate distance. Correspondingly, for the same interplate distance, the height of the peaks increases with increasing ε_{wp}.

The profiles of ρ_z become different as D increases to 10 Å. When D = 10 Å and ε_{wp} = 0.2 kcal/mol, each of the main peaks in ρ_z shows a shoulder at around z = ±2.3 Å. The shoulder grows into a subpeak when ε_{wp} = 0.3 kcal/mol and D = 10 Å. The height of the subpeak continues to grow as ε_{wp} increases to 0.5 and 0.7 kcal/mol, while the location of the subpeak remains

the same. When D = 10 Å and ε_{wp} = 0.7 kcal/mol, the heights of the subpeaks are equivalent to the heights of the main peaks, which are located at z = ±1.4 Å. The split of each single peak into two subpeaks indicates that at D = 10 Å, the ice state becomes a puckered bilayer ice (referred to as the 2U structure[12]).

The profiles of ρ_z of liquid states of systems with ε_{wp} = 0.2 and 0.7 kcal/mol, with interplate distances D = 8 and 10 Å, are shown in Figure 9, along with the profiles of the corresponding ice states. The profiles of ρ_z of the liquid states have much wider distributions with smaller peaks at each layer center and with nonzero density across the slit center, indicating that water molecules in liquid states can move between two layers across the slit center, while the transverse movements of water molecules in the solid states are highly restricted. In the liquid state, as the water–plate interaction parameter, ε_{wp}, increases from 0.2 to 0.7 kcal/mol, the wetting of the plate increases, and the probability of water visiting the center of the nanoslit decreases.

Direct comparison of the ice configuration of the systems with D = 8 and 10 Å and ε_{wp} = 0.7 kcal/mol is shown in Figure 10. The top views of ices at both D = 8 and 10 Å exhibit similar hexagonal ice structure, with two layers in register. However, the side views clearly show that the bilayer structure of the ice at D = 8 Å is flat whereas the bilayer at D = 10 Å exhibits a puckered structure. Increasing the interplate separation and volume induces a transition between flat and puckered solid ice phases. The flat bilayer ice at D = 8 Å allows each molecule to have four hydrogen-bonded neighbors. The top and side views of the bilayer ice structure at D = 8 Å demonstrate that the angle of neighbors within one layer is roughly 120° and the angle assumed by neighbors not all in one layer is roughly 90°.

The puckered bilayer structure at D = 10 Å results in external sublayers with three hydrogen-bonded neighbors, while the molecules on the inner sublayers have four hydrogen-bonded neighbors. Each layer of the puckered bilayer structure at D = 10 Å is split into an external sublayer and an internal sublayer. In Figure 10, the molecules of the external sublayers of the puckered structure are dark blue, and those of the internal sublayers are red. A pattern is observed with one dark blue molecule surrounded by three red molecules and one red molecule surrounded by three dark blue molecules. The two layers are packed such that red molecules stack over red molecules, allowing water molecules on the upper and lower layers to be close enough to form hydrogen bonds. Each red molecule forms three hydrogen bonds within the layer and a forth hydrogen bond with the closest red molecule on the adjacent layer. This is different from the "pleated sheet water" (PSW),[29] which, having "ridges" stacking over "ridges" and "valleys" stacking over "valleys", does not allow water molecules of different layers to share hydrogen bonds.

Distributions of angles between hydrogen-bonded neighbors of ice structures at D = 8 and 10 Å are shown in Figure 11. Consistent with the impression made by inspection of the structures, the angle distribution of the ice structure at D = 8 Å has two peaks located near 120 and 90°, corresponding to the angles formed within one layer and between two layers. These results agree with previous simulations[12] of ice structures at D = 8 Å as well as experimental determination.[53] The angle distribution of the ice structure at D = 10 Å, formed by angles for molecules with four or three hydrogen-bonded neighbors, has a single peak located near 109°, which is the signature value of tetrahedral geometry. As bulk ice Ih is characterized by
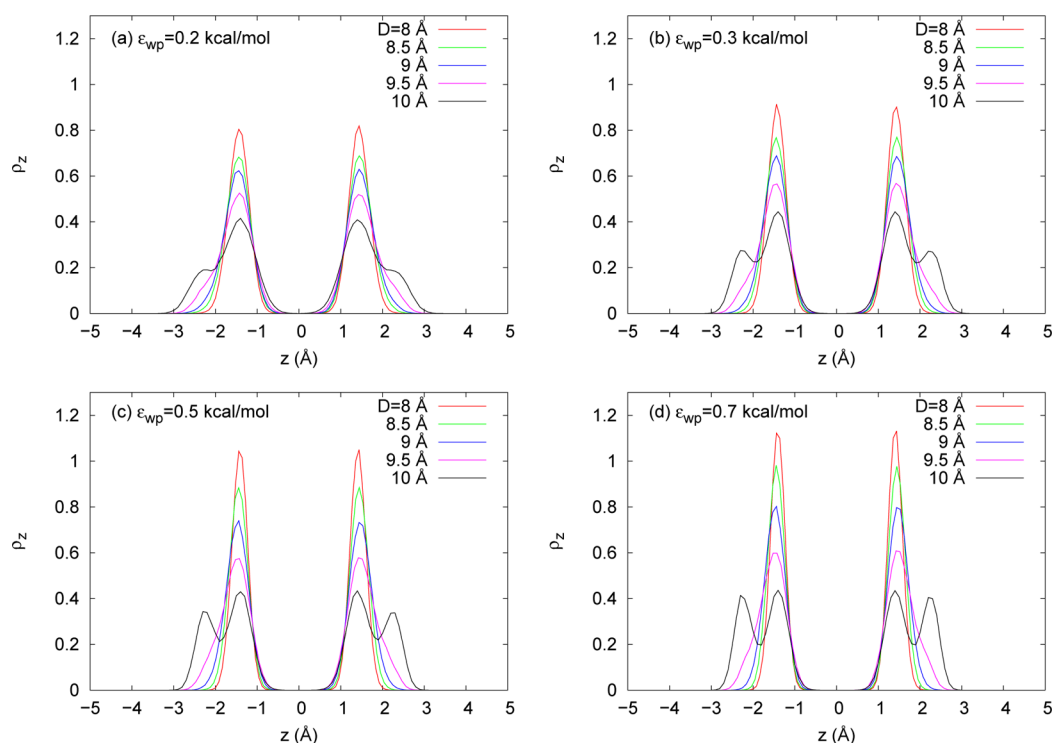
Figure 8. (a–d) TPDs, ρ_z, of ice structures of systems with four different water–plate interaction parameters, $\varepsilon_{wp} = 0.2, 0.3, 0.5,$ and 0.7 kcal. Each subfigure compares ρ_z of systems with varying interplate distances, $D = 8, 8.5, 9, 9.5,$ and 10 Å, but the same water–plate interaction parameter, ε_{wp}, and 256 water molecules. The TPDs for systems with 1024 water molecules are shown in the Supporting Information.
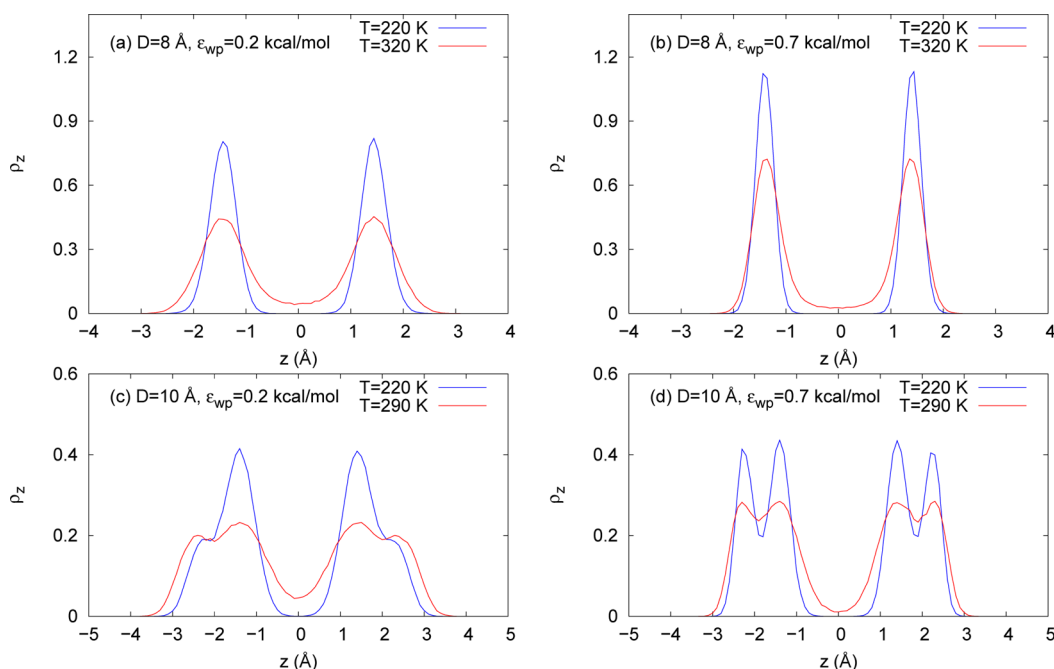

Figure 9. (a,b) TPDs, ρ_z, of systems with $D = 8$ Å and $\varepsilon_{wp} = 0.2$ and 0.7 kcal, respectively. (c,d) ρ_z of systems with $D = 10$ Å and $\varepsilon_{wp} = 0.2$ and 0.7 kcal, respectively. The systems have 256 water molecules.

hexagonal symmetry and near-tetrahedral bonding angles, we recognize that the ice structure at $D = 10$ Å is equivalent to a slice of ice Ih. Figure 11 also displays fragments of the ice structures at $D = 8$ and 10 Å, composed of three adjacent rings in both layers, which accentuate the flat hexagonal ring structure at $D = 8$ Å and the puckered hexagonal ring structure at $D = 10$ Å.

■ CONCLUSIONS

We investigated the phase behavior of water nanofilms confined between parallel atomistic plates at atmospheric lateral pressure using a coarse-grained mW model. The solid-to-liquid phase transition of water nanofilms was simulated with gREM to provide comprehensive sampling in the vicinity of the first-order phase transition for plates of varying separation and
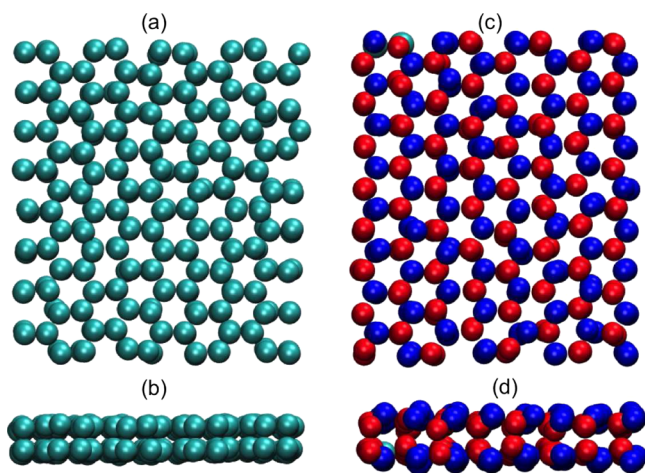
Figure 10. (a) Top view of a bilayer ice structure of a system with 256 water molecules; $D = 8$ Å and $\varepsilon_{wp} = 0.7$ kcal/mol at 220 K. (b) Side view of the same structure. The water molecules are colored cyan. (c,d) The top and side views of the bilayer ice structure of a system with $D = 10$ Å and $\varepsilon_{wp} = 0.7$ kcal/mol at 220 K. The water molecules on the outer sublayers are colored dark blue, those on the inner sublayers are colored red, and the rest are colored cyan.
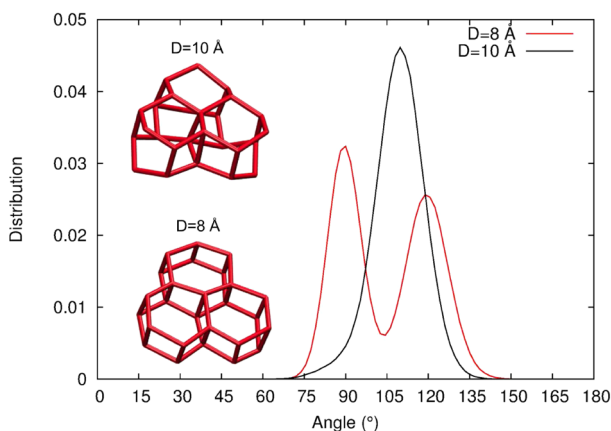

Figure 11. Distributions of angles formed by hydrogen-bonded neighbors in ice structures with 256 water molecules at $D = 8$ (red) and 10 Å (black) with $\varepsilon_{wp} = 0.7$ kcal/mol and $T = 220$ K. Fragments of the ice structure for $D = 8$ and 10 Å are inserted, showing three adjacent rings in both layers.

strength of attraction from strongly hydrophobic to strongly hydrophilic.

The transition temperature reaches a maximum at interplate separation $D = 8.5$ Å, at all water–plate interaction strengths, and behaves parabolically as a function of interplate distance, in agreement with previous results.[12] At a given interplate distance D, the transition temperature is highest when the plates are most hydrophilic, showing that for water nanofilms confined between parallel plates, the transition temperature is a sensitive function of the geometry and physical nature of the nanoconfining environment. The melting transition temperature of the water nanofilm was observed to span a remarkably wide range of values from 240 to 340 K, with varying parameters for the interplate distance and water–plate interaction.

For interplate distances between 8 and 10 Å, the water nanofilm forms a bilayer structure for the liquid and solid ice states. Ice structures for D between 8 and 9.5 Å are flat bilayers

composed of planar hexagonal rings with nontetrahedral angles, while bilayer ice at $D = 10$ Å takes on a puckered structure, similar to a slab of bulk ice Ih, characterized by hexagonal symmetry and near-tetrahedral bonding angles. The puckered bilayer ice was previously reported,[12] but it was observed to be unstable with low melting temperature (210 K) at 1 atm of lateral pressure, with the instability induced by the hydrophobic plate.

In this study, the stable puckered ice bilayer structure with high melting temperature (275 K) was obtained for an interplate distance of 10 Å and hydrophilic confining plates. This confining environment provides adequate volume to accommodate the tetrahedral angles and stabilization of undercoordinated water molecules of the external sublayers. As such, hydrophilic plates are observed to stabilize the puckered bilayer ice, which was otherwise marginally stable in the featureless hydrophobic environment. Further work employing different forms of water–plate potential, including the introduction of a directional hydrogen-bonding interaction, would verify the observed dependence of the phase behavior of water nanofilms on the nature of the nanoconfining environment.

■ ASSOCIATED CONTENT

Ⓢ Supporting Information

The Supporting Information is available free of charge on the ACS Publications website at DOI: 10.1021/acs.jpcb.5b10481.

> Enthalpy, $H(T)$, isobaric heat capacity, $C_p(T)$, and transverse density profiles, ρ_z, for systems with 1024 water molecules, $\varepsilon_{wp} = 0.2, 0.3, 0.5$, and 0.7 kcal/mol, and varying interplate separations, D (PDF)

■ AUTHOR INFORMATION

Corresponding Author

*E-mail: straub@bu.edu.

Notes

The authors declare no competing financial interest.

■ REFERENCES

(1) Berendsen, H. J.; Grigera, J. R.; Straatsma, T. P. The missing term in effective pair potentials. *J. Phys. Chem.* **1987**, *91*, 6269−6271.

(2) Jorgensen, W. L.; Chandrasekhar, J.; Madura, J. D.; Impey, R. W.; Klein, M. L. Comparison of simple potential functions for simulating liquid water. *J. Chem. Phys.* **1983**, *79*, 926−935.

(3) Mahoney, M. W.; Jorgensen, W. L. A five-site model for liquid water and the reproduction of the density anomaly by rigid, nonpolarizable potential functions. *J. Chem. Phys.* **2000**, *112*, 8910−8922.

(4) Rick, S. W.; Stuart, S. J.; Berne, B. J. Dynamical fluctuating charge force fields: Application to liquid water. *J. Chem. Phys.* **1994**, *101*, 6141−6156.

(5) Wallqvist, A.; Berne, B. J. Effective potentials for liquid water using polarizable and nonpolarizable models. *J. Phys. Chem.* **1993**, *97*, 13841−13851.

(6) Chen, B.; Xing, J. H.; Siepmann, J. I. Development of polarizable water force fields for phase equilibrium calculations. *J. Phys. Chem. B* **2000**, *104*, 2391−2401.

(7) Ren, P.; Ponder, J. W. Polarizable atomic multipole water model for molecular mechanics simulation. *J. Phys. Chem. B* **2003**, *107*, 5933−5947.

(8) Moore, E. B.; Molinero, V. Growing correlation length in supercooled water. *J. Chem. Phys.* **2009**, *130*, 244505.

(9) Le, L.; Molinero, V. Nanophase segregation in supercooled aqueous solutions and their glasses driven by the polyamorphism of water. *J. Phys. Chem. A* **2011**, *115*, 5900−5907.

(10) Moore, E. B.; Molinero, V. Structural transformation in supercooled water controls the crystallization rate of ice. *Nature* **2011**, *479*, 506−508.

(11) Reinhardt, A.; Doye, J. P. K. Free energy landscapes for homogeneous nucleation of ice for a monatomic water model. *J. Chem. Phys.* **2012**, *136*, 054501.

(12) Kastelowitz, N.; Johnston, J. C.; Molinero, V. The anomalously high melting temperature of bilayer ice. *J. Chem. Phys.* **2010**, *132*, 124511.

(13) Moore, E. B.; Allen, J. T.; Molinero, V. Liquid-Ice Coexistence below the Melting Temperature for Water Confined in Hydrophilic and Hydrophobic Nanopores. *J. Phys. Chem. C* **2012**, *116*, 7507−7514.

(14) Johnston, J. C.; Kastelowitz, N.; Molinero, V. Liquid to quasicrystal transition in bilayer water. *J. Chem. Phys.* **2010**, *133*, 154516.

(15) DeMille, R. C.; Cheatham, T. E.; Molinero, V. A Coarse-Grained Model of DNA with Explicit Solvation by Water and Ions. *J. Phys. Chem. B* **2011**, *115*, 132−142.

(16) Nguyen, A. H.; Molinero, V. Stability and metastability of bromine clathrate polymorphs. *J. Phys. Chem. B* **2013**, *117*, 6330−6338.

(17) Han, S.; Choi, M. Y.; Kumar, P.; Stanley, H. E. Phase transitions in confined water nanofilm. *Nat. Phys.* **2010**, *6*, 685−689.

(18) Bai, J.; Zeng, X. C. Polymorphism and polyamorphism in bilayer water confined to slit nanopore under high pressure. *Proc. Natl. Acad. Sci. U. S. A.* **2012**, *109*, 21240−21245.

(19) Bakulin, A. A.; Cringus, D.; Pieniazek, P. A.; Skinner, J. L.; Jansen, T. L. C.; Pshenichnikov, M. S. Dynamics of Water Confined in Reversed Micelles: Multidimensional Vibrational Spectroscopy Study. *J. Phys. Chem. B* **2013**, *117*, 15545−15558.

(20) Perez, C.; Muckle, M. T.; Zaleski, D. P.; Seifert, N. A.; Temelso, B.; Shields, G. C.; Kisiel, Z.; Pate, B. H. Structures of Cage, Prism, and Book Isomers of Water Hexamer from Broadband Rotational Spectroscopy. *Science* **2012**, *336*, 897−901.

(21) Stanley, H. E.; Mishima, O. The relationship between liquid, supercooled and glassy water. *Nature* **1998**, *396*, 329−335.

(22) Errington, J. R.; Debenedetti, P. G.; Torquato, S. Cooperative Origin of Low-Density Domains in Liquid Water. *Phys. Rev. Lett.* **2002**, *89*, 215503.

(23) Kumar, P.; Buldyrev, S. V.; Starr, F. W.; Giovambattista, N.; Stanley, H. E. Thermodynamics, structure, and dynamics of water confined between hydrophobic plates. *Phys. Rev. E* **2005**, *72*, 051503.

(24) Koga, K.; Tanaka, H. Phase diagram of water between hydrophobic surfaces. *J. Chem. Phys.* **2005**, *122*, 104711.

(25) Koga, K.; Tanaka, H.; Zeng, X. C. First-order transition in confined water between high-density liquid and low-density amorphous phases. *Nature* **2000**, *408*, 564−567.

(26) Giovambattista, N.; Rossky, P. J.; Debenedetti, P. G. Phase transitions induced by nanoconfinement in liquid water. *Phys. Rev. Lett.* **2009**, *102*, 050603.

(27) Zangi, R.; Mark, A. E. Monolayer ice. *J. Chem. Phys.* **2003**, *119*, 1694−1700.

(28) Koga, K.; Gao, G. T.; Tanaka, H.; Zeng, X. C. Formation of ordered ice nanotubes inside carbon nanotubes. *Nature* **2001**, *412*, 802−805.

(29) Anick, D. J. Atypical water lattices and their possible relevance to the amorphous ices: A density functional study. *AIP Adv.* **2013**, *3*, 042119.

(30) Chodankar, S.; Perret, E.; Nygard, K.; Bunk, O.; Satapathy, D. K.; Espinosa Marzal, R. M.; Balmer, T. E.; Heuberger, M.; van der Veen, J. F. Density profile of water in nanoslit. *Europhys. Lett.* **2012**, *99*, 26001.

(31) Lu, Q.; Kim, J.; Farrell, J. D.; Wales, D. J.; Straub, J. E. Investigating the solid-liquid phase transition of water nanofilm using the generalized replica exchange method. *J. Chem. Phys.* **2014**, *141*, 18C525.

(32) Kim, J.; Keyes, T.; Straub, J. E. Generalized Replica Exchange Method. *J. Chem. Phys.* **2010**, *132*, 224107.

(33) Geyer, C. J.; Thompson, A. Annealing Markov-chain Monte Carlo with applications to ancestral inference. *J. Am. Stat. Assoc.* **1995**, *90*, 909−920.

(34) Sugita, Y.; Okamoto, Y. Replica-exchange molecular dynamics method for protein folding. *Chem. Phys. Lett.* **1999**, *314*, 141−151.

(35) Hukushima, K.; Nemoto, K. Exchange Monte Carlo method and application to spin glass simulations. *J. Phys. Soc. Jpn.* **1996**, *65*, 1604−1608.

(36) Kamberaj, H.; van der Vaart, A. Multiple scaling replica exchange for the conformational sampling of biomolecules in explicit water. *J. Chem. Phys.* **2007**, *127*, 234102.

(37) Hansmann, U. H. E. Parallel tempering algorithm for conformational studies of biological molecules. *Chem. Phys. Lett.* **1997**, *281*, 140−150.

(38) Mitsutake, A.; Sugita, Y.; Okamoto, Y. Generalized-ensemble algorithms for molecular simulations of biopolymers. *Biopolymers* **2001**, *60*, 96−123.

(39) Wales, D. J.; Berry, R. S. Coexistence in Finite Systems. *Phys. Rev. Lett.* **1994**, *73*, 2875−2878.

(40) Andricioaei, I.; Straub, J. E. Generalized simulated annealing algorithms using Tsallis statistics: Application to conformational optimization of a tetrapeptide. *Phys. Rev. E: Stat. Phys., Plasmas, Fluids, Relat. Interdiscip. Top.* **1996**, *53*, R3055−R3058.

(41) Andricioaei, I.; Straub, J. E. On Monte Carlo and molecular dynamics methods inspired by Tsallis statistics: Methodology, optimization, and application to atomic clusters. *J. Chem. Phys.* **1997**, *107*, 9117−9124.

(42) Li, H.; Li, G.; Berg, B. A.; Yang, W. Finite reservoir replica exchange method to enhance sampling on rugged energy surfaces. *J. Chem. Phys.* **2006**, *125*, 144902.

(43) Lu, Q.; Kim, J.; Straub, J. E. Solid-liquid phase transition of Dzugutov model using gREM. *J. Phys. Chem. B* **2012**, *116*, 8654−8661.

(44) Lu, Q.; Kim, J.; Straub, J. E. Order parameter free enhanced sampling of the vapor-liquid transition. *J. Chem. Phys.* **2013**, *138*, 104119.

(45) Cho, W. J.; Kim, J.; Lee, J.; Keyes, T.; Straub, J. E.; Kim, K. S. Limit of metastability for liquid and vapor phases of water. *Phys. Rev. Lett.* **2014**, *112*, 157802.

(46) Lupi, L.; Kastelowitz, N.; Molinero, V. Vapor deposition of water on graphitic surfaces: formation of amorphous ice, bilayer ice, ice I and liquid water. *J. Chem. Phys.* **2014**, *141*, 18C508.

(47) Malolepsza, E.; Kim, J.; Keyes, T. Entropic description of gas hydrate ice-liquid equilibrium via enhanced sampling of coexisting phases. *Phys. Rev. Lett.* **2015**, *114*, 170601.

(48) Kim, J.; Keyes, T.; Straub, J. E. Communication: Iteration-free, weighted histogram analysis method in terms of intensive variables. *J. Chem. Phys.* **2011**, *135*, 061103.

(49) Frenkel, D.; Smit, B. *Understanding Molecular Simulation: From Algorithms to Applications*; Academic Press, Inc.: Orlando, FL, 1996.

(50) Ferrenberg, A. M.; Swendsen, R. H. Optimized Monte Carlo data analysis. *Phys. Rev. Lett.* **1989**, *63*, 1195−1198.

(51) Rizzi, L. G.; Alves, N. A. Multicanonical entropy like-solution of STWHAM. *J. Chem. Phys.* **2011**, *135*, 141101.

(52) Church, M.; Ferry, C.; van Giessen, A. E. Thermodynamics of peptide dimer formation. *J. Chem. Phys.* **2012**, *136*, 245102.

(53) Kimmel, G. A.; Matthiesen, J.; Baer, M.; Mundy, C. J.; Petrik, N. G.; Smith, R. S.; Dohnalek, Z.; Kay, B. D. No Confinement Needed: Observation of a Metastable Hydrophobic Wetting Two-Layer Ice on Graphene. *J. Am. Chem. Soc.* **2009**, *131*, 12838−12844.